sustainability

MDPI

Article

Estimating Three-Dimensional Permeability Distribution for Modeling Multirate Coreflooding Experiments

Evans Anto-Darkwah [1], Takeshi Kurotori [2], Ronny Pini [3] and Avinoam Rabinovich [1,*]

[1] School of Mechanical Engineering, Tel-Aviv University, Tel-Aviv 69978, Israel
[2] Department of Energy Science and Engineering, Stanford University, Stanford, CA 94305, USA
[3] Department of Chemical Engineering, Imperial College London, London SW7 2AZ, UK
* Correspondence: avinoamr@tauex.tau.ac.il

Abstract: Characterizing subsurface reservoirs such as aquifers or oil and gas fields is an important aspect of various environmental engineering technologies. Coreflooding experiments, conducted routinely for characterization, are at the forefront of reservoir modeling. In this work, we present a method to estimate the three-dimensional permeability distribution and characteristic (intrinsic) relative permeability of a core sample in order to construct an accurate model of the coreflooding experiment. The new method improves previous ones by allowing to model experiments with mm-scale accuracy at various injection rates, accounting for variations in capillary–viscous effects associated with changing flow rates. We apply the method to drainage coreflooding experiments of nitrogen and water in two heterogeneous limestone core samples and estimate the subcore scale permeability and relative permeability. We show that the models are able to estimate the saturation distribution and core pressure drop with what is believed to be sufficient accuracy.

Keywords: drainage coreflooding; permeability map; capillary heterogeneity; subcore scale; multirate coreflooding; CO_2 storage; energy storage in aquifers

Citation: Anto-Darkwah, E.; Kurotori, T.; Pini, R.; Rabinovich, A. Estimating Three-Dimensional Permeability Distribution for Modeling Multirate Coreflooding Experiments. *Sustainability* **2023**, *15*, 3148. https://doi.org/10.3390/su15043148

Academic Editors: Seyed M. Shariatipour and Mohammadreza Bagheri

Received: 2 December 2022
Revised: 30 January 2023
Accepted: 3 February 2023
Published: 9 February 2023

1. Introduction

Subsurface reservoirs such as aquifers or oil and gas fields have the potential of playing a major role in environmental technologies of the upcoming years. CO_2 geological storage [1,2] is currently conducted at various reservoirs worldwide and may become much more common with increasing efforts of reducing anthropogenic CO_2 emissions. Aquifer contamination is a growing problem, and in situ remediation methods are being used and developed [3–6]. Subsurface reservoirs have been used for gas storage for many years [7,8], and recently, a new technology for energy storage, based on gas injection in reservoirs, has been developed [9,10]. All of the above technologies require reservoir characterization and flow modeling as a fundamental step for feasibility studies, project planning, evaluation and monitoring. Some common methods of reservoir characterization are pumping tests, borehole characterization, well testing and conducting coreflooding experiments.

Coreflooding experiments consist of injecting fluids into small porous rock samples taken from a reservoir (core sample), while monitoring the pressure drop and saturation. It is becoming more common to combine these experiments with computed tomography (CT) imaging so that a 3D map of saturation can be generated during the flow experiment. Analysis of these experiments can provide a characterization of the rock on the scale of a millimeter throughout the entire sample. This is expressed by obtaining the 3D spatially varying subcore (millimeter-scale) properties: permeability (k), porosity (ϕ), capillary pressure (P_c) and characteristic relative permeability function (k_r^{char}). The latter is also known as intrinsic relative permeability and may differ from the core (effective) relative permeability curves due to capillary effects. Obtaining these properties on the subcore level is important for a number of reasons. First, it allows to investigate

the impact of subcore heterogeneity on the core-scale flow and to characterize capillary trapping [11–18]. Furthermore, the accurate numerical simulations of core flow [19,20] can be used to replace expensive and cumbersome experiments. Finally, the relation between fine-scale (subcore) and effective (core-scale) properties can be studied and used to develop upscaling methods [21–25].

In real world applications, the flow properties estimated in coreflooding experiments are upscaled and used in field-scale models. This is the primary purpose of these experiments and the reason why effective properties, representing the entire core sample, are typically the focus of core analysis. However, the effective properties depend on the conditions applied in the experiments, in particular the flow rate of the injected fluids. As flow rate is reduced, capillary effects become more influential and phenomena such as capillary trapping occur [13,17,26–30], leading to changes in effective relative permeability (k_r^{ef}) and capillary pressure (P_c^{ef}) [20,31]. Therefore, it is important to carry out coreflooding experiments at different flow rates in order to investigate the rate dependence of the effective properties and to find subcore-scale properties which are not rate-dependent. An accurate subcore model will allow to estimate effective properties of the core at different flow rates using numerical simulations instead of experiments.

A method for modeling coreflooding with millimeter-scale accuracy was first developed in the last decade [32–34]. The method is based on assuming the Leverett *J*-function [35] relationship between subcore scale P_c and core P_c^{ef}. Then, the spatially varying subcore permeability (k) and characteristic curves (k_r^{char}) are estimated by inversion of this relationship in an iterative procedure until an accurate match of numerical simulation with experimental results is obtained for both saturation (determining k) and pressure drop (determining k_r^{char}). The method was developed for drainage coreflooding and recently extended to imbibition as well [36]. A similar approach was presented by other authors [37–39] in recent years, with the main difference that k is taken to be constant and only P_c curves are spatially varying. The work by [39] predicts the 3D saturations at different flow rates for carbonate rocks but takes a data-driven approach rather than solving the governing equations. Furthermore, the method does not predict the overall pressure drop at steady state for different flow rates.

In this work, we apply the method of characteristic curve and permeability estimation [36] to data from experiments on two limestone core samples, conducted at a number of injection flow rates. The experiments considered are of drainage coreflooding at 100% nonwetting phase (N_2) injection. The estimation procedure is modified to accommodate the limited data, i.e., a single flow fraction, and takes advantage of the data from multiple injection rates. The properties obtained using the new, modified procedure are used as input in coreflooding numerical simulations. The models are shown to reproduce the experimental results with sufficiently high accuracy, comparable to what was found in previous similar investigations.

The novelty of this work is as follows. First, we extend the method of k and k_r^{char} estimation [36] to limestone rocks. Second, we consider only 100% nonwetting phase injection using steady-state data, which provide limited information for nonwetting phase relative permeability and no information for water relative permeability. Third, we combine data from multiple experiments with different injection rates. The models are therefore shown to be capable of accurately capturing the transition between cases of varying capillary–viscous effects, as expressed by the changing capillary number with flow rate. Finally, we note that the construction of accurate 3D coreflooding models has not been thoroughly investigated yet and more studies, such as this one, are important for establishing this approach.

We note that although the experiments in this work consist of N_2 and water flow, and our model assumes immiscible fluids in an incompressible medium, the method and model described here are generally applicable to any two fluids. For example, similar methods and models have been applied to the flow of supercritical CO_2 and brine [36,40], and this is important in advancing the application of CO_2 storage in saline aquifers. We further

believe the procedure can be applied to oil–water or other gas–water flows pertaining to additional applications.

The paper is structured as follows. In Section 2, we present the new modified method for estimating k and k_r^{char} given data from multirate experiments. In Section 3, we present experiments conducted on two limestone core samples along with an initial analysis of the data and an implementation of the method from Section 2. Section 4 presents the results for application of the method and a comparison of the final model results with the experimental data for accuracy evaluation. A summary and the main conclusions are given in Section 5.

2. Method

In this section, we present the new procedure for estimating the 3D permeability map $k(x, y, z)$ and characteristic relative permeability functions: $k_{w,r}^{\text{char}}(S_w)$, $k_{nw,r}^{\text{char}}(S_w)$ of a core sample. We assume that N steady-state coreflooding experiments were carried out with varying total injection rates of Q_N, Q_2, ..., Q_1, where Q_N is the lowest rate and Q_1 is the highest rate, so that $Q_1 > Q_2 > ... > Q_N$. Each experiment consists of drainage of a fully wetting-phase-saturated core by injection of 100% of the nonwetting phase. Using X-ray CT images, we obtain the porosity of the core $\phi(x, y, z)$ and the steady-state saturation distribution $S_w^{Q_i}(x, y, z)$ for each flow rate Q_i $(1 < i < N)$. Additionally, pressure drop Δp^{Q_i} along the core at steady-state flow conditions is measured for each flow rate Q_i. Furthermore, a single-phase coreflooding experiment is conducted to determine the effective permeability k^{ef} of the sample. Finally, we carry out additional experiments, such as mercury intrusion tests, to obtain capillary pressure data $P_c(S_w)$ for the core sample.

Figure 1 presents a schematic drawing detailing the steps of the proposed method. The first step entails gathering the experimental data, determining the irreducible water saturation S_{wi} and fitting an analytical function to the P_c data obtained from mercury intrusion tests. We generally fit the P_c curve by first removing any experimental capillary pressure results that are below the smallest saturation value obtained in the coreflooding experiments, i.e., the smallest value in $S_w^{Q_1}(x, y, z)$. The remaining data points are fitted with a curve, thus determining S_{wi}, capillary entry pressure (P_e) and any other fitting parameters. The second step (denoted 'Step II' in Figure 1) entails applying the iterative method [33,40] for determining $k(x, y, z)$ and k_r^{char} separately for each flow rate. This is briefly summarized in the following.

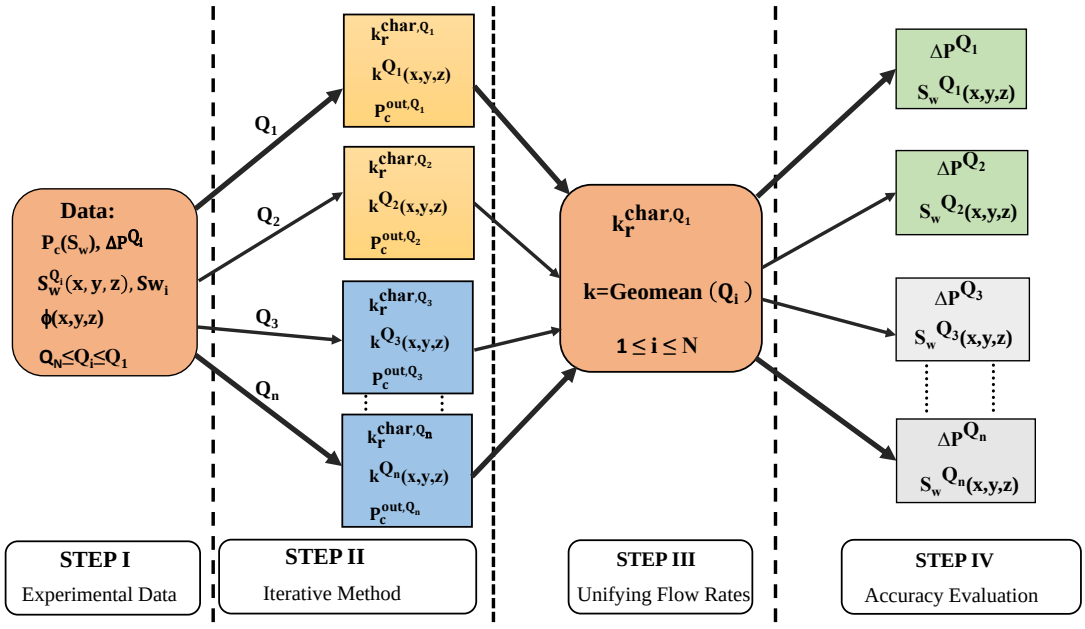

Figure 1. Flow chart of the procedure for k and k_r^{char} estimation.

The iterative method consists of the following stages.
(1) Determining an initial permeability distribution by the equation:

$$k_j = \kappa \frac{\phi_j}{\overline{P}_c^2} \frac{k^{\mathrm{ef}}}{\langle \phi \rangle} \left[P_e J(\widetilde{S}_{w,j}) \right]^2, \tag{1}$$

where subscript j denotes a property of a voxel or grid block in the discretized 3D core sample, $J(\widetilde{S}_w)$ is the Leverett J-function fitted to the capillary pressure data, P_e is capillary entry pressure, $\langle \phi \rangle$ is the core average porosity, $\overline{P}_c$ is the slice average capillary pressure, κ is a scaling factor which ensures that the effective permeability (obtained from a single-phase simulation) matches the experimentally determined value and

$$\widetilde{S}_w = (S_w - S_{wi})/(1 - S_{wi}) \tag{2}$$

is the normalized saturation. The saturation $\widetilde{S}_{w,j}$ for each voxel j is obtained from the experimental saturation maps. Equation (1) is at the heart of the method and is obtained directly from the empirical Leverett scaling relationship for capillary pressure, i.e., $P_c(k, \phi, S_w) = \sqrt{\langle \phi \rangle k / (k^{\mathrm{ef}} \phi)} P_e J(\widetilde{S}_w)$, and the experimental capillary pressure curve is fitted with the function $P_c = P_e J(\widetilde{S}_w)$.

(2) The second stage involves estimating the characteristic relative permeability by implementing the method detailed in a previous work [40]. The $k_r^{\mathrm{char}}(S_w)$ curves are assumed to be uniform in the core and of the form given by a chosen analytical function. This function has some fitting parameters, which are determined by matching the experimentally measured pressure drop with those from single-phase flow simulations (the problem reduces to solving single-phase flow equations after substituting the experimentally measured saturation distribution in the governing equations; see [40] for more details). In this work, we consider only 100% nonwetting phase injection and, therefore, our measured pressure drop is only for the nonwetting phase, i.e., we cannot obtain $k_{r,w}^{\mathrm{char}}$ directly. We therefore assume that the fitting parameters obtained for $k_{r,nw}^{\mathrm{char}}$ are the same for $k_{r,w}^{\mathrm{char}}$ [41]. Furthermore, we note that there is only one pressure drop measurement used for obtaining k_r^{char} for each flow rate, as opposed to the multiple measurements usually available when considering experiments with varying injection fluid fraction.

(3) The third stage includes conducting two-phase flow coreflooding simulations using initially estimated k and k_r^{char}. These simulations assume that the fluids are immiscible and that both rock and fluids are incompressible. Furthermore, the core outlet capillary pressure must be modeled correctly. Previous investigators [42,43] have described the existence of capillary pressure discontinuity at the core outlet, where fluids exit. To account for this phenomenon, also known as the end effect in coreflooding analysis, the outer boundary P_c is posed as zero [37,44]. However, this leads to significant underestimation of nonwetting phase saturation near the core outlet. Recently, [45] showed that the end effects could impact large portions of the core and therefore can lead to erroneous nonwetting phase numerical prediction. Therefore, we take the approach of [33] to impose a capillary pressure value (P_c^{out}) such that the average saturation in the outlet slice from numerical simulations matches that obtained by experimental saturation. After running the simulation, the accuracy of estimated properties is determined by comparison of simulated output saturation (S_{nw}^{sim}) with experimental saturation ($S_{nw}^{\mathrm{Q_i}}$) obtained via CT scans. This is quantified by a simple equation:

$$err = \frac{1}{M} \sum_j |S_{nw,j}^{\mathrm{sim}} - S_{nw,j}^{\mathrm{Q_i}}|, \tag{3}$$

where M is the total number of grid blocks. When the error is less than a threshold value (err = 0.01 and 0.025 were used here), the procedure is terminated, and the estimated k and k_r^{char} are obtained. However, if the error remains higher than the threshold value, we conduct stages 1–3 again by calculating a new k using Equation (1) with simulation

output $P_{c,j}$ for each voxel j replacing the average value $\overline{P}_c$. Then, k_r^{char} and P_c^{out} are updated accordingly, and new two-phase simulations are conducted with the newly estimated properties. This is repeated in an iterative manner until Equation (3) is less than the threshold.

Step III in Figure 1 is an amalgamation of the results of of Step II. After step II, we obtain k^{Q_i}, $k_{w,r}^{\text{char,Q_i}}$ and $k_{nw,r}^{\text{char,Q_i}}$ for each flow rate Q_i; while in principle these should all be the same, in reality they are not due to errors in experiments, simulation and the iterative estimation method. Therefore, we take the geometric mean of the permeability:

$$k_i = (k_i^{Q_1} \cdot k_i^{Q_2} \cdots k_i^{Q_N})^{1/N} \tag{4}$$

as the permeability representing the core and use only $k_r^{\text{char,Q}_1}$. The latter is applicable if flow rate Q_1 is sufficiently high so that the viscous limit is reached, in which the characteristic curve is also the effective curve. A second option is to average all characteristic curves as follows:

$$k_r^{\text{char}} = \frac{1}{N}(k_r^{\text{char,Q}_1} + k_r^{\text{char,Q}_2} + \ldots + k_r^{\text{char,Q}_N}). \tag{5}$$

For the value of P_c^{out}, we use the highest flow rate value, i.e., P_c^{out,Q_1}. This concludes the estimation part of the method.

In the last step of the method, we evaluate the accuracy of the final model in estimating the saturation distribution and pressure drop of all the experiments (see Step IV in Figure 1). Simulations are conducted using the final k and k_r^{char} functions obtained in Step III for all flow rates, and the results are compared with the experimental data to assess the accuracy of the model.

3. Experimental Data and Application of Method

Data used in this work are obtained from experiments already discussed in detail in previous publications [46,47] and summarized below. A series of multirate steady-state coreflooding experiments were conducted on two limestone samples, namely, Indiana (Kocurek Industries Inc., Caldwell, TX, USA) and Ketton (Ketton Quarry, Rutland, UK). The experiments were conducted using a medical CT scanner to obtain the saturation distribution when the flow reached steady state. The core samples were kept at a temperature of 20 °C and a pressure of 3 MPa using nitrogen as the nonwetting phase and water as the wetting phase [46]. Much of the rock and fluid properties are summarized in Table 1. The fractional flow of N_2 injection for all the experiments was taken to be 100%. The viscosity of N_2 at the specified experimental conditions is 1.8×10^{-5} Pa·s and the gas–water viscosity ratio of 0.02 was considered for all experiments. The core porosity (Figure 2a,d) and N_2 saturation three-dimensional maps (examples in Figure 2b,c,e,f) were obtained from CT image analysis applying well-established methods [48]. Steady-state pressure at the inlet and outlet of the core were measured using high-precision pressure transducers for each experiment so that the pressure drop over the sample was recorded. Using the multiphase Darcy law, effective relative permeability points can be computed from the pressure drops and the core average saturation obtained from the CT image analysis. These are plotted for each rock in Figure 3a,b. Pressure drops are also measured during a single-phase flow experiment to obtain the effective permeability of each sample, as presented in Table 1.

Mercury intrusion capillary pressure (MICP) data were obtained from small samples of each rock with representative elementary volumes of 2–3 cm^3. This is similar to the volume of each 2 mm-thick slice of the rock samples used in the coreflooding experiments [46,47]. The data are fitted with a function and plotted for each rock in Figure 4a,b (denoted 'MICP' in the legend), as is further explained in the next section. An additional P_c curve estimation is taken from the previous literature [46], carried out using a 1D model via an in-house optimization workflow routine by history matching the experimental saturation profiles and pressure drop values for all tested flow rates. This is also plotted for each rock in Figure 4a,b (denoted '1D model' in the legend). Additional details on the experimental

procedures and protocols are presented extensively elsewhere [46,47]. We also note that, to reduce capillary end effects, the last 1.2 cm of the core data pertaining to the Indiana limestone was removed from this analysis, following the approach taken in the previous literature for this rock sample [39].

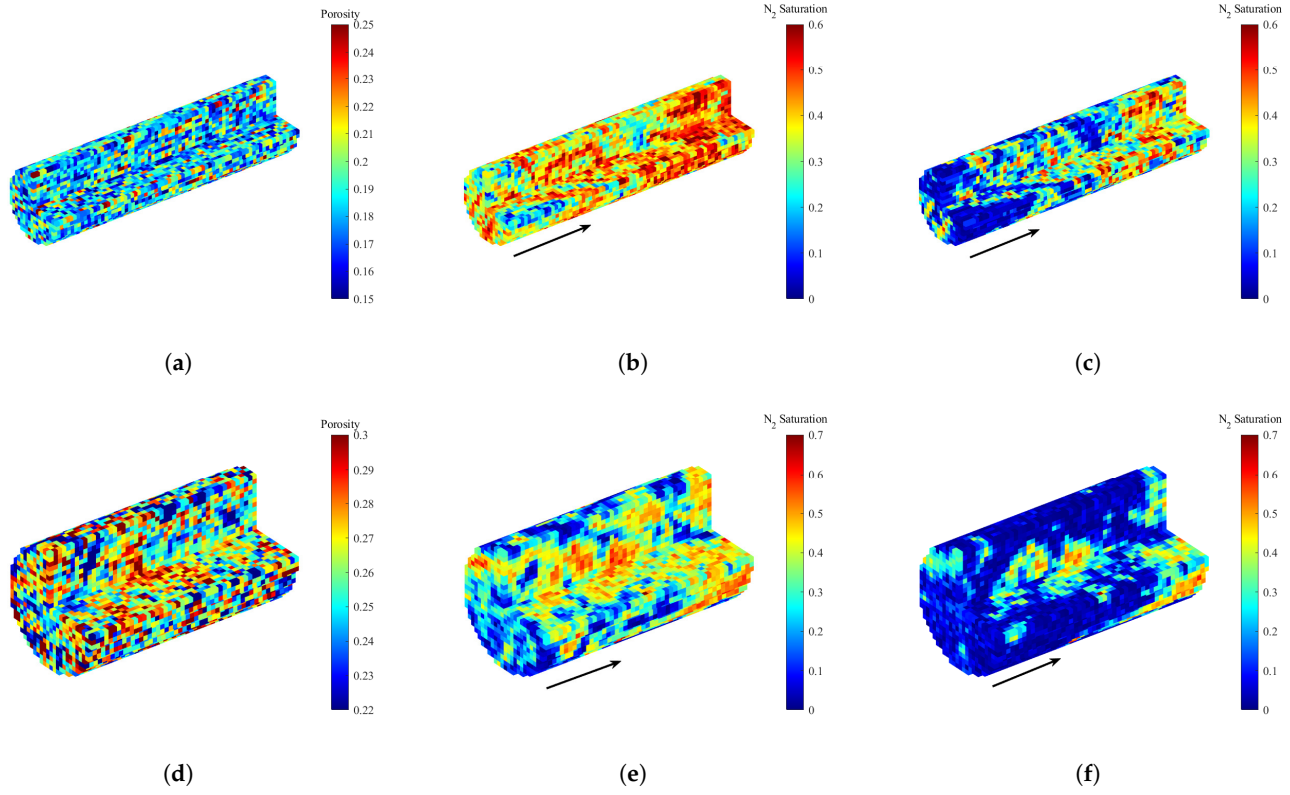

Figure 2. Experimental maps of porosity (ϕ^{CT})—(**a**,**d**), high flow rate N_2 saturations ($S_{N_2}^{CT}$)—(**b**,**e**) and low flow rate N_2 saturations ($S_{N_2}^{CT}$) —(**c**,**f**) for Indiana (**top row**) and Ketton (**bottom row**) cores. (**a**) Indiana Porosity. (**b**) Indiana 40 mL/min. (**c**) Indiana 1.5 mL/min. (**d**) Ketton Porosity. (**e**) Ketton 60 mL/min. (**f**) Ketton 2 mL/min.

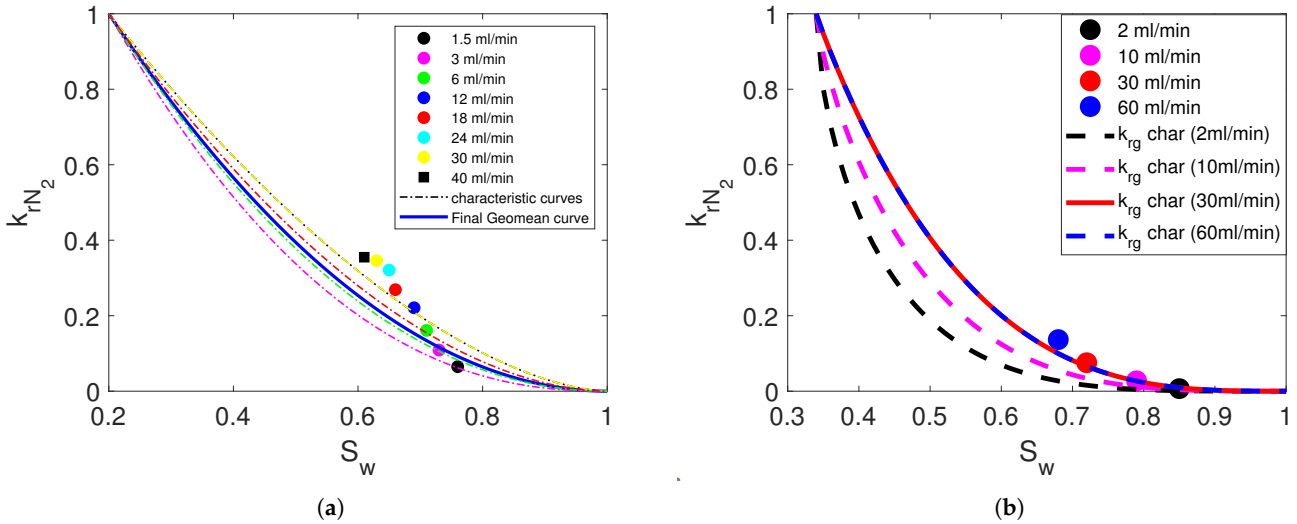

Figure 3. Nonwetting phase effective and characteristic relative permeability curves. (**a**) Indiana. (**b**) Ketton.

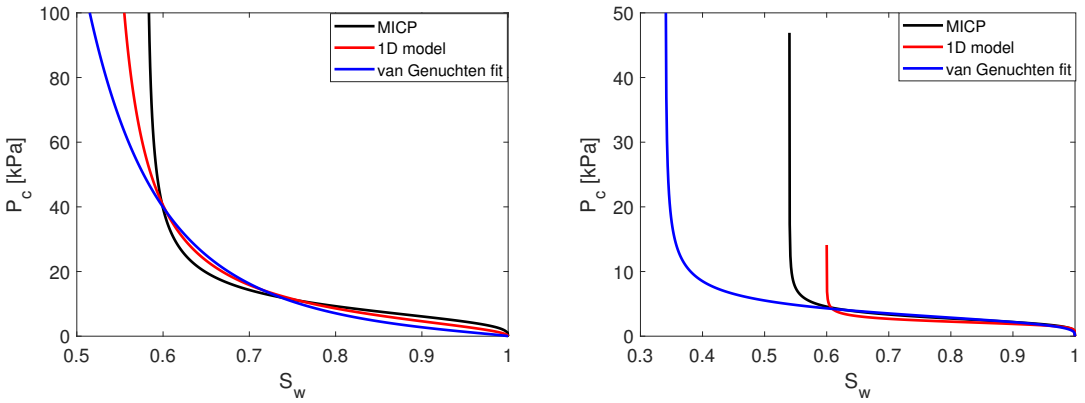

Figure 4. Experimental capillary pressure (MICP), history-matched capillary pressure (1D model) and van Genuchten fit to MICP data. (**a**) Indiana. (**b**) Ketton.

Table 1. Core and fluid experimental properties.

Property	Indiana	Ketton
Core length (cm)	15	10
Core diameter (cm)	3.8	5
Average porosity, Φ	0.20	0.27
Effective permeability (mD)	80	1900
Nitrogen viscosity (Pa·s)	1.8×10^{-5}	1.8×10^{-5}
Irreducible water saturation (S_{wi})	0.20	0.34
MICP fitting parameters (α, m, S_{wi})	0.13, 0.65, 0.58	0.37, 0.79, 0.54
1D model fitting parameters (α, m, S_{wi})	0.17, 0.48, 0.52	0.46, 0.85, 0.60
van Genuchten fitting parameters (α, m, S_{wi})	0.33, 0.21, 0.20	0.31, 0.71, 0.34
Nitrogen fractional flow	100%	100%
Injection flow rates tested (mL/min)	1.5, 3, 6, 12, 18, 24, 30, 40	2, 10, 30, 60

3.1. Application of Method

In this section, we follow the steps described in Section 2 to estimate the permeability distribution and characteristic relative permeability of each core sample. As described in Step I of the procedure (Figure 1), we first gather the experimental data which were already detailed in the beginning of Section 3: $\phi(x,y,z)$, $S_w^{Q_i}(x,y,z)$, $P_c(\widetilde{S}_w)$ and Δp^{Q_i}. Next, we determine S_{wi} and fit the capillary pressure data. The MICP data are fitted with a van Genuchten-type [49] function as follows:

$$P_c(\widetilde{S}_w) = \frac{1}{\alpha}\left(\widetilde{S}_w^{-1/m} - 1\right)^{1-m}, \tag{6}$$

where α and m are the fitting parameters detailed in Table 1. The irreducible saturation S_{wi} is also a fitting parameter in Equation (6), as it appears in $\widetilde{S}_w$ (see Equation (2)). The capillary pressure curves found in this approach for both rocks are presented in Figure 4a,b, denoted by "MICP".

The values of $S_{wi} = 0.58$ and 0.54, pertaining to the MICP curve, represent the entire cores and are much too large for the analysis of subcore properties. In fact, permeability estimation is not possible for any mm-scale voxel with a saturation smaller than S_{wi}. We therefore take a different approach, which calls for assigning S_{wi} the minimum water saturation value out of all the experiments. These values were chosen from the highest flow rate experiments for both rocks, i.e., 40 mL/min and 60 mL/min for Indiana and Ketton, respectively. We then found $S_{wi} = 0.20$ and 0.34 for Indiana and Ketton, respectively, from the steady-state-measured N_2 saturation data. Then, knowing the S_{wi} a priori, we fit the MICP data of both rocks with the van Genuchten model of Equation (6), where only α and m are fitting parameters. The capillary pressure curves found in this approach for both rocks are presented in Figure 4a,b, denoted by "van-Genuchten fit" and are the curves used in the following analysis. A third P_c curve is plotted for reference in Figure 4a,b and denoted "1D model". These curves are taken from a previous work [46], where a 1D model was history-matched to the coreflooding data without the use of the MICP data. It can be seen that all three curves are very similar up until a deviation, which occurs at low saturation due to the different S_{wi} values.

We continue the data description by elaborating more on the models used in the calculation of effective and characteristic relative permeability curves, found in Figure 3. The effective relative permeability points for both rock samples were calculated using the well-known Darcy two-phase law for subsurface flows by substituting the steady state experimentally measured pressure drop Δp^{Q_i} and average saturation $\left\langle S_w^{Q_i}(x,y,z)\right\rangle$ from the 3D CT saturation maps. The application of Darcy's equation leads to a relative permeability point for each of the tested flow rates, as shown in Figure 3a,b. However, due to the rate dependence of the points, we cannot simply connect them to obtain a relative permeability curve. Instead, we must seek the characteristic curve for each flow rate which leads to the correct effective point, which is part of the iterative method detailed in Step II of Section 2 (see Figure 1). We assume the characteristic curves are expressed by the following equation, taken to be the same as in previous investigations of these two rocks [46], i.e.,

$$k_{r,N_2}^{\text{char}} = \left(1 - \widetilde{S}_w^2\right)\left(1 - \widetilde{S}_w^{1/n_1}\right)^{n_1} \tag{7a}$$

$$k_{r,w}^{\text{char}} = \widetilde{S}_w^2\left[1 - (1 - \widetilde{S}_w)^{1/n_1}\right]^{n_1}, \tag{7b}$$

where n_1 is the fitting parameter. In fitting the effective relative permeability points for Indiana limestone rock, we found that Equation (7a,b) is not appropriate, as the m tends to zero for all flow rates. Therefore, for the Indiana rock, we adopted the Brooks–Corey function [50] of the form:

$$k_{rN_2}^{\text{char}} = 1 - (\widetilde{S}_w)^{n_2} \tag{8a}$$

$$k_{r,w}^{\text{char}} = (\widetilde{S}_w)^{n_2}, \tag{8b}$$

where n_2 is the fitting parameter.

The procedure in Step II of Section 2 (see Figure 1) was conducted next. In each iteration of the method, k_r^{char} curves of the form given by Equation (7) for Ketton and Equation (8) for Indiana are used as input curves in our two-phase flow simulations. The powers n_1 and n_2 are obtained by matching single-phase flow simulation output and experimental effective relative permeability points [34]. The curves are assumed uniform throughout the core. In Figure 3a,b, we do not plot the k_{rw}^{char} curves, since we do not have laboratory data for them. However, since we assume the k_{rw}^{char} have the form of Equations (7b) and (8b), and the fitting powers are the same as those of k_{r,N_2}^{char}, we are able to generate the corresponding curves to incorporate into our numerical simulations.

All two-phase flow simulations in this study were conducted using the Stanford University General Purpose Research Simulator [51]. We used the fully implicit black-oil numerical model, assigning N_2 properties to the oil phase and water properties to the water

phase. Rock and fluid properties were incorporated as incompressible, in line with previous models. The resolution of the grids were taken to be the same as that of the experimental saturation and porosity maps from the CT scans. Additional inlet and outlet slices were added to the original grids to ensure uniform injection and distribution of fluids at the core inlet and also to account for accurate fluid saturations at the core exit. The inlet slice is assigned with constant permeability and perforated in all blocks with N_2 injection wells. The outlet slice blocks are assigned a constant P_c^{out} and perforated with production wells producing at a constant pressure. The respective simulation grid resolution and sizes used in our studies are: 74 × 20 × 20 blocks with dimensions of 1.9 mm × 1.9 mm × 2.0 mm in the x × y × z directions for Indiana limestone and 51 × 27 × 27 blocks with dimensions of 1.9 mm × 1.9 mm × 2.0 mm for Ketton. Rock properties used in our numerical simulations are as stated in Table 1. The densities of N_2 and water used are 34.7 and 987 kg/m^3, respectively.

The iterative procedure in Step II of the method (see Figure 1) is carried out for each flow rate separately. The accuracy of the estimated properties at the end of each iteration is determined by comparison of simulated output saturation ($S_{N_2}^{\text{sim}}$) with experimental saturation ($S_{N_2}^{\text{CT}}$). This is quantified by using Equation (3). When the error is less than a threshold value ($err = 0.025$ and 0.01 for Indiana and Ketton, respectively), the procedure is terminated, and the estimated k and k_r^{char} are obtained. However, if the error remains higher than the threshold value, a new k is estimated using the inverse capillary pressure–permeability relationship (Equation (1)) with simulation P_c as input, then k_r^{char} and P_c^{out} are updated accordingly and new two-phase simulations are conducted with the newly estimated properties. Overall, we conducted three and ten two-phase flow iterations for the Indiana and Ketton rocks, respectively. Each iteration lasted for 3 h for Indiana and 1 h for Ketton.

The final result for $k_{rN_2}^{\text{char}}$ is plotted in Figure 3a,b in dashed lines, and the powers n_1, n_2 are presented in Table 2. Although, in theory, there should be one characteristic curve which is responsible for different effective curves, depending on the flow rate (due to varying capillary–viscous effects), it can be seen that each flow rate resulted in a different characteristic curve. In the case of the Ketton rock, the two highest flow rates resulted in the same characteristic curve, which also passes in close proximity to the effective points. We assume that this is an expression of the convergence of the curves to the viscous limit. We therefore continue by using the characteristic curve obtained in the analysis of the highest flow rate, i.e., the 60 mL/min experiment, as part of Step III of the method (see Figure 1). For the case of the Indiana rock, a similar convergence was observed for 30 and 40 mL/min. However, we found that the average of the relative permeability curves, as given by Equation (5), gives a better result in our model, particularly for the lower flow rate cases. The converged values for P_c^{out} are also presented in Table 2 for each flow rate.

We continue to carry out Step III of the method (see Figure 1), which entails unifying the results to obtain a single model for all flow rates. A final permeability is calculated by taking the geometric mean of all the converged $k(x, y, z)$, which were obtained for each flow rate in the iterative procedure. This, together with the k_r^{char} and P_c^{out} of the highest flow rates completes the model. We perform one final two-phase numerical simulation for each flow rate with our unified model to predict the saturations of all the tested flow rates. This final simulation is used for Step IV (see Figure 1) of validating the model and assessing the accuracy by comparing with the experimental results, both qualitatively and quantitatively.

Table 2. Parameters n_1/n_2, P_c^{out} and error E_M for the converged models of each flow rate.

Flow Rate (mL/min)	$k_{rN_2}^{char}$ Power (n_1/n_2)	P_c^{out}	E_M
Indiana			
1.5	2.84	8.5×10^{-3}	0.05
3	2.31	3.5×10^{-4}	0.04
6	2.07	1.5×10^{-4}	0.03
12	1.88	7.0×10^{-6}	0.04
18	1.84	2.5×10^{-6}	0.053
24	1.59	2.0×10^{-6}	0.045
30	1.65	3.5×10^{-6}	3.5×10^{-5}
40	1.65	2.5×10^{-6}	0.03
Ketton			
2	1.82	0.38	2.8×10^{-5}
10	1.45	0.46	2.8×10^{-5}
30	1.09	1.10	5.60×10^{-5}
60	1.09	0.54	8.40×10^{-5}

4. Results

Figure 5 presents two examples of the converged model considering a single experiment of a given flow rate. It can be seen that the model obtained for 60 mL/min for the Ketton Limestone (Figure 5a,b) is almost perfectly accurate, with both slice average saturation and block-by-block saturation having an excellent match between simulation and experiment. This is in line with previous results for drainage modeling of sandstone rocks [22,40]. The converged model for Indiana Limestone also has a high accuracy with a match of the slice average saturation (Figure 5c) and block-by-block saturation (Figure 5d), however, some errors can be seen in the latter. It is apparent that the Indiana rock experiment was slightly more difficult to model than the Ketton one. In fact, for Indiana, convergence of the criteria given by Equation (3) was slightly larger, taken to be 0.025 instead of 0.01. A number of factors can be attributed to this lower accuracy: more heterogeneity of the sample, a larger difference between core overall residual water saturation and grid block S_{wi} (see Table 1), as well as more difficulty in matching the capillary pressure and relative permeability curves.

An additional measure of error is used in this work, defined as the number of grid blocks with a saturation difference larger than 0.05 divided by the total number of grid blocks, i.e., $E_M = M_T/M$, where $M_T = \sum_{j=1}^{M} M_j$ and $M_j = 1$ if $|S_{N_2,j}^{\text{sim}} - S_{N_2,j}^{\text{CT}}| > 0.05$, or 0 otherwise ($M$ is the total number of grid blocks, and j denotes a grid block). This measure is referred to as the error (E_M) of the simulation and represents the agreement with experimental results. The value of 0.05 was arbitrarily chosen, however, choosing a different value will not change the conclusions discussed in the following. The error is indicated in the bottom plots of Figure 5b,c and in Table 2. It can be seen that, in general, the error is much larger for the Indiana rock in comparison with the Ketton, though both are very small. Table 2 also shows the P_c^{out} factor and the powers of the characteristic curves (n_1 in Equation (7) for Ketton and n_2 in Equation (8) for Indiana) for each converged model of a particular flow rate experiment.

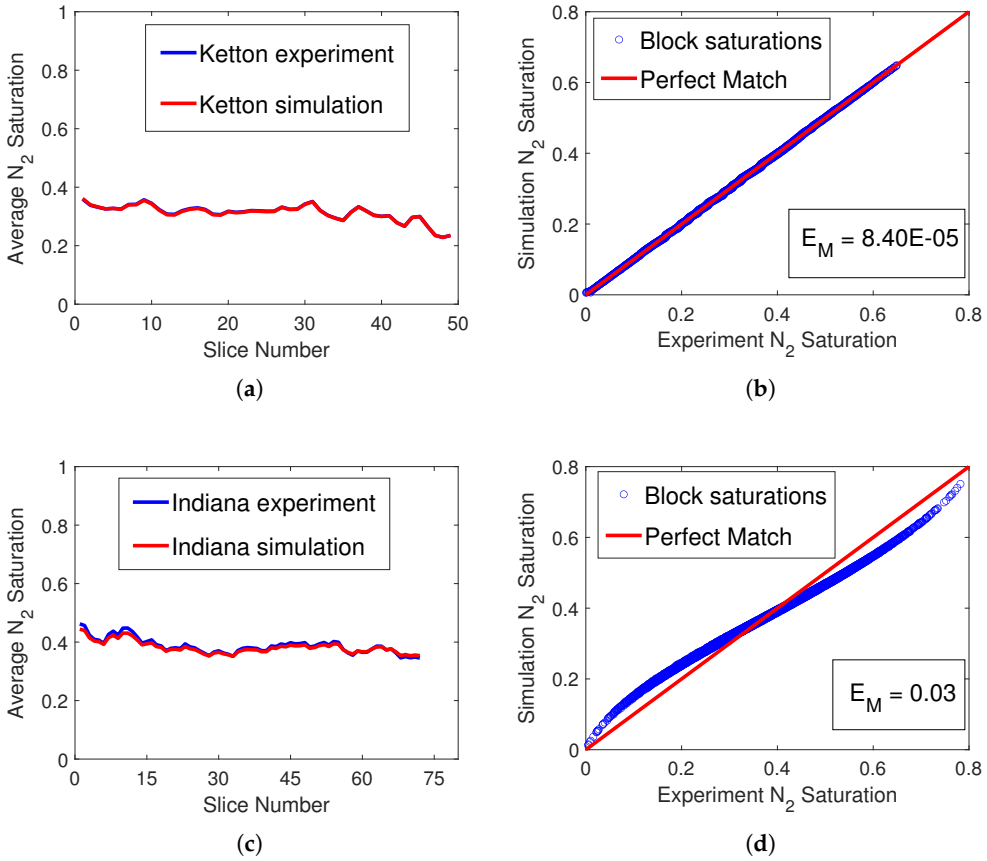

Figure 5. High flow rate saturation outputs for iterative procedure. (**a**) Ketton 60 mL/min. (**b**) Ketton 60 mL/min. (**c**) Indiana 40 mL/min. (**d**) Indiana 40 mL/min.

Figure 6 presents the final estimated permeability for both limestone rocks. Figure 6a,c has three-dimensional maps of the permeability in the core plugs. It is apparent that the Ketton rock is much more permeable than the Indiana, and it has particularly high permeability structures at the second half of the sample, whereas the Ketton has a more evenly distributed heterogeneity. This is also apparent in the probability density functions (PDF) of $\ln k$, shown in Figure 6b,d, where the Indiana rock has a typical lognormal distribution, whereas the Ketton has a somewhat bimodal distribution pertaining to the low- and high-permeability zones seen in Figure 6a. Figure 6b,d presents the final permeability (geometric mean) PDFs alongside the PDF of each flow rate separately. It can be seen that the k estimations have very similar distributions between the different flow rates, which is a positive result, indicating robustness, since in reality there is a single k for each core, regardless of the experiment flow rate. We can also observe the high heterogeneity of the Indiana rock, with a $\ln k$ variance of around 3.5, whereas the Ketton rock is much less heterogeneous with a $\ln k$ variance of around 0.6.

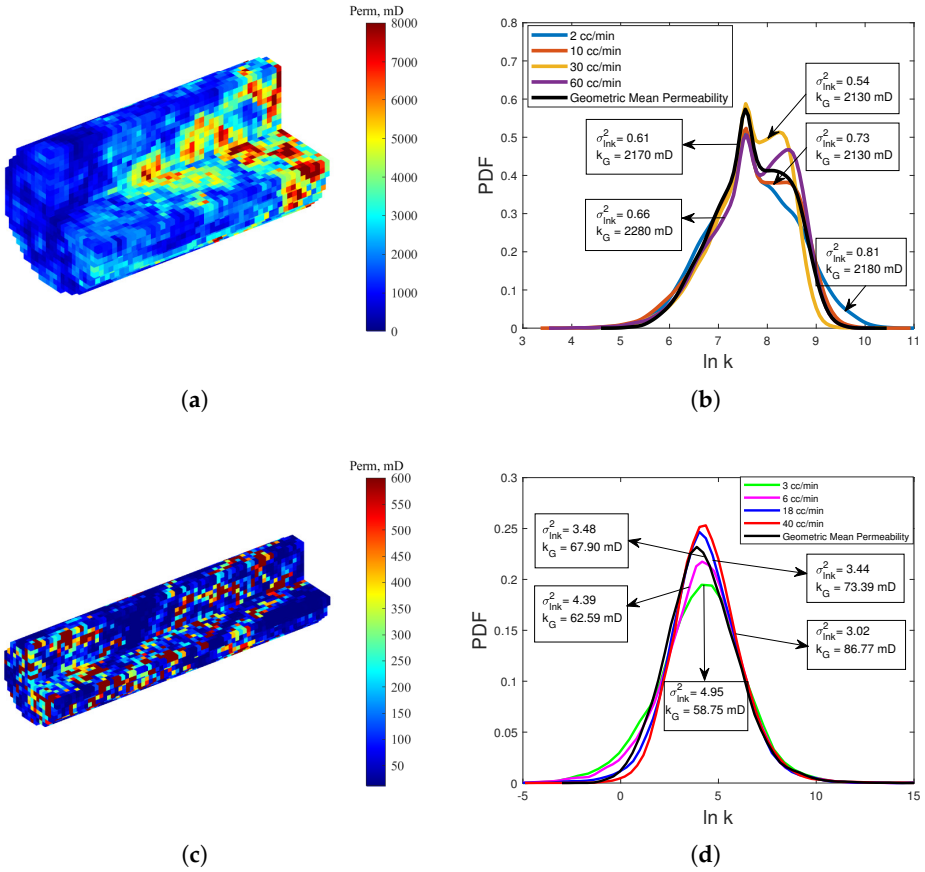

Figure 6. Geomean permeability and PDF. (**a**) Ketton permeability map. (**b**) Ketton probability density function of ln k. (**c**) Indiana permeability map. (**d**) Indiana probability density function of ln k.

Figure 7 presents the results for the final multirate model of the Ketton core sample. Comparing Figure 7d,h with Figure 5a,b, it can be seen that there is a large difference in the accuracy of the single-rate and multirate models. The block-by-block comparison between the simulations and experiments shows a general agreement, however, errors for many blocks are significant and E_N = 0.22–0.32, indicating 22–32% of the blocks have saturation errors larger than 0.05. Nevertheless, the slice average saturation of the model matches that of the experiment with sufficient accuracy (Figure 5a–d), and the trends are captured, suggesting that heterogeneity is represented well by the simulations. The model prediction of the pressure drop along the core for each flow rate is presented in Table 3, in comparison with the experimentally measured Δp^{Q_i}. It can be seen that the pressure drop predicted by the simulations for the Ketton rock is in good agreement with the experiment measurements with errors of only 4–20%.

Table 3. Simulations and laboratory pressure drop for each flow rate.

Flow Rate (mL/min)	Experiment ΔP (psi)	Simulation ΔP (psi)	Error in ΔP (%)	CapillaryNumber (N_c)
Indiana				
1.5	1.61	1.33	17	0.008
3	1.93	1.33	31.0	0.009
6	2.61	1.91	27	0.013
12	3.80	2.95	22	0.018
18	4.68	3.13	33	0.022
24	5.23	4.89	7	0.025
30	6.06	5.85	3	0.029
40	7.89	7.41	6	0.038
Ketton				
2	0.31	0.24	20	0.11
10	0.38	0.32	16	0.14
30	0.42	0.39	7	0.15
60	0.46	0.44	4	0.17

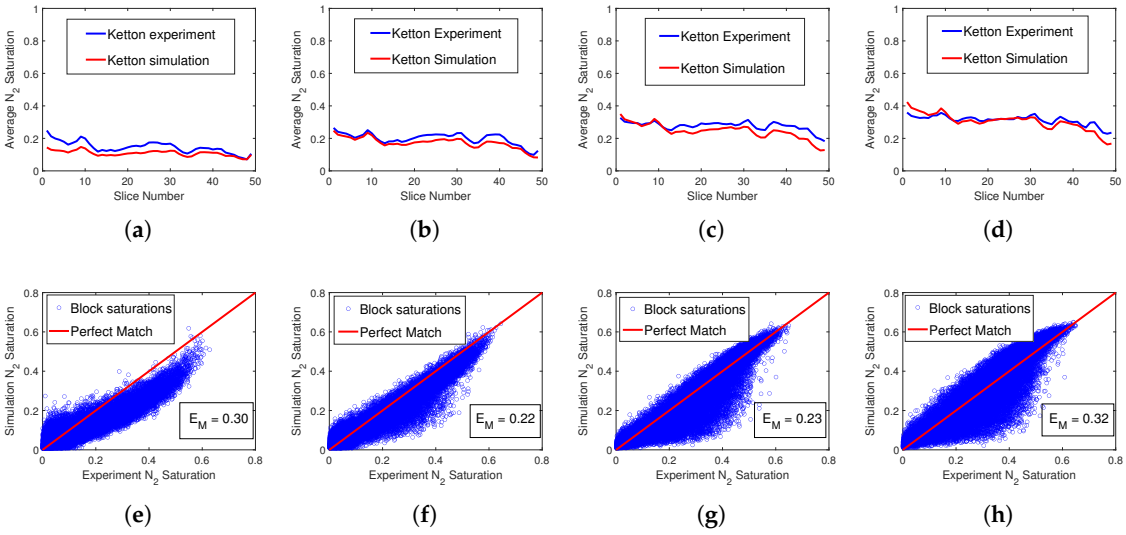

Figure 7. Ketton Geomean saturation output. (**a**) 2 mL/min. (**b**) 10 mL/min. (**c**) 30 mL/min. (**d**) 60 mL/min. (**e**) 2 mL/min. (**f**) 10 mL/min. (**g**) 30 mL/min. (**h**) 60 mL/min .

Figures 8 and 9 present the results for the final multirate model for the Indiana core sample, considering the low-rate and high-rate simulations, respectively. For high flow rates of 12–40 mL/min, a very good match between simulations and experiments can be seen for both slice average saturation (Figures 8d and 9a–d) and block-by-block saturation (Figures 8h and 9e–h). The overall error is also fairly low, varying in the range of E_M = 0.15–0.18. The low-flow-rate simulations of 1.5–6 mL/min are less accurate, showing a larger mismatch with block saturation (Figure 8e–g) and a visible mismatch for the slice average curves (Figure 8a–c). Nevertheless, the trends in saturation variations appear to be captured, as seen in Figure 8a–c. The overall errors for the low-rate simulations are reasonable and in the range of E_M = 0.24–0.37, similar to those of the Ketton rock. In terms of core pressure drop, results are presented in Table 3. The high-flow-rate experiments of 24–40 mL/min are predicted very well by the model with errors of 3–7%, while the lower flow rate cases of 1.5–18 mL/min have slightly larger errors of 17–33%.

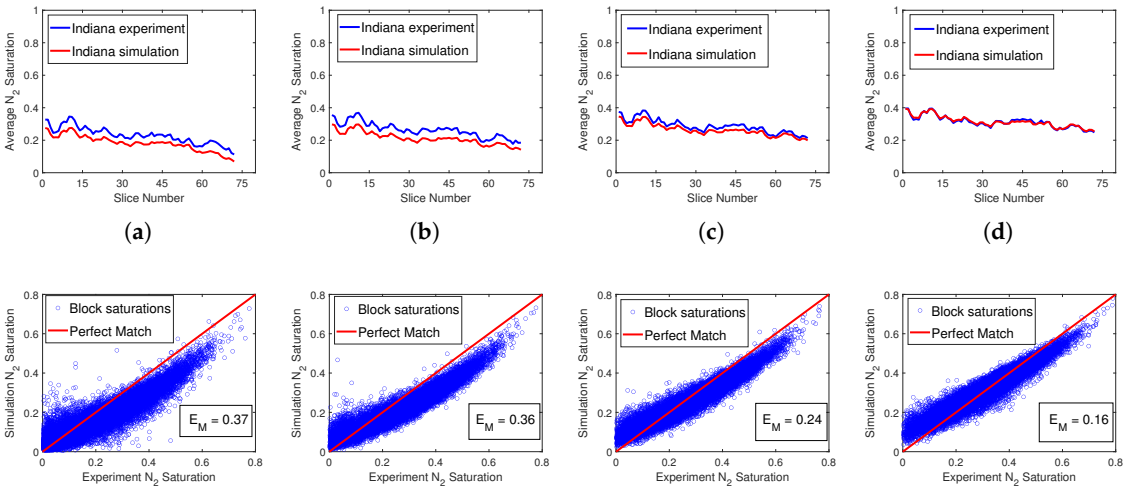

Figure 8. Low flow rate: Indiana Geomean saturation output. (**a**) 1.5 mL/min. (**b**) 3 mL/min. (**c**) 6 mL/min. (**d**) 12 mL/min. (**e**) 1.5 mL/min. (**f**) 3 mL/min. (**g**) 6 mL/min. (**h**) 12 mL/min.

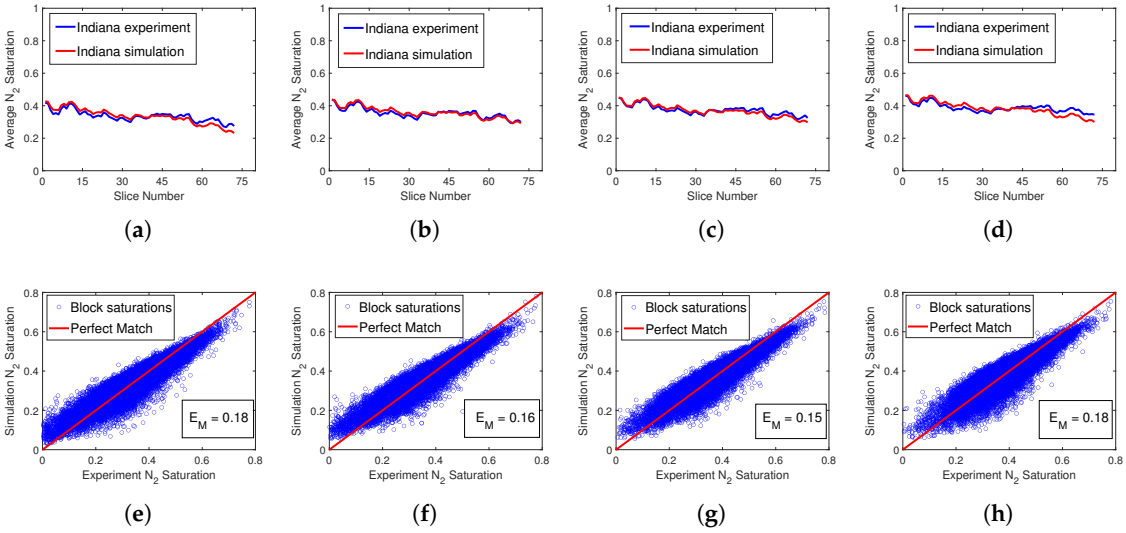

Figure 9. High flow rate: Indiana Geomean saturation output. (**a**) 18 mL/min. (**b**) 24 mL/min. (**c**) 30 mL/min. (**d**) 40 mL/min. (**e**) 18 mL/min. (**f**) 24 mL/min. (**g**) 30 mL/min. (**h**) 40 mL/min.

An interesting result is that the errors of the converged simulations for each flow rate did not necessarily predict the error for the final multirate model error for that flow rate. For example, the best overall results are for the Indiana rock for flow rates of 12–40 mL/min, where errors of E_M = 0.15–0.18 were found (Figures 8h and 9e–h). However, this is not expected if we observe the converged model for these flow rates, since they generally have large errors when compared with the Ketton rock (see Table 2), as discussed previously. It appears that the dominating factor determining the model accuracy for saturation distribution is the variation in the predicted k maps. This occurs due to a combination of errors which arise during the k estimation, i.e., experimental errors and inconsistencies, numerical errors and errors associated with the method itself. It can be seen in Figure 6b that, for Ketton, there is indeed a large variation in the PDF of $\ln k$ between the different flow rates. This variation is associated with the high-permeability structure which is seen for the high flow rates and does not appear for low rates. The more k variations with flow rate would mean that the final geometric mean k will most likely have less accuracy.

On the other hand, much less variation is seen in the PDFs of the Indiana rock (Figure 6d) between different flow rates, indicating higher accuracy of the final geometric mean k.

The larger errors observed for low flow rates in the Indiana experiments (Figure 8e–g) could be attributed to the significant change in P_c^{out}, seen in Table 2 for 1.5–6 mL/min. The jump in P_c^{out} for low rates seen in Table 2 indicates that a larger value is required to match the outlet saturation and, since we use the P_c^{out} of the highest flow rate, it can be regarded as the dominating factor for the increase in error for these rates (E_M = 0.24–0.37).

The last column in Table 3 shows the capillary number N_c associated with each experiment. It is calculated in a similar manner to the previous literature [23,52], as the core pressure drop divided by the core capillary pressure drop, i.e., $N_c = \Delta p / \Delta P_c$, where Δp is given in the second column of the table, and ΔP_c is calculated by averaging P_c over the inlet and outlet and subtracting the two. Since ΔP_c was found to have hardly any variations with flow rate for Ketton and slight variations for Indiana (which is believed to be due to end effects), we take average values for each rock. Thus, ΔP_c = 2.76 and 208 were used for Ketton and Indiana, respectively. As can be seen, the values of N_c increase with flow rate, which is expected due to the more dominant viscous effects. For Ketton, N_c increases by only a factor of about 1.5, while for Indiana, it increases by a factor of 5. The values of N_c ranging from 0.008 to 0.17 are in a regime in which both capillary and viscous effects are influential, leaning towards a capillary dominating regime for the lower values [53]. The errors of the model cannot in general be correlated with N_c because of the many factors contributing to the errors, including numerical errors [54] and the variation of k maps, which was discussed previously. The capillary number is influenced by many parameters, such as fluid viscosities, fluid fraction, flow rate and capillary pressure function. The parameters influencing the capillary number N_c are all encapsulated in the ratio of pressure drop and capillary pressure drop in our calculation. We note that, in this work, the capillary number changes are mostly related to flow rate changes, and further work can be conducted in the future by systematically varying fluid or rock properties.

5. Summary and Conclusions

This work presented a workflow for constructing a model which is able to predict multirate coreflooding experiments, thus improving existing procedures. The workflow assumes that drainage experiments have been conducted with only 100% nonwetting phase injection at different injection rates. Therefore, the usual effective relative permeability data obtained at different injection fluid fractions is not available. We apply the new workflow on two core plug samples of Ketton and Indiana limestones to obtain the characteristic relative permeability curves, capillary pressure curves and three-dimensional permeability maps. The final model is then validated by comparing the simulation results to the experimental data. We show that the simulations are able to capture the saturation variations associated with heterogeneity that are presented in the experiments. In general, the agreement between experiments and the model saturation are reasonable. The accuracy of the model varies between flow rates and is most accurate for the high flow rates of the Indiana experiments (18–40 mL/min). The model is also able to accurately predict the core pressure drop in most cases with errors of 3–33%. Overall, the model was able to capture the saturation and pressure changes with varying flow rate, i.e., for a range of capillary numbers.

Overall, we find that the main challenge is the transition from a model of a single experiment to one that can accurately match results from a number of experiments, in this case different flow rates. This is in line with previous findings [40] when experiments of different injection fluid fractions were modeled. However, a significant difference is that in this work we consider the same outlet capillary pressure factor P_c^{out} for all experiments of the same rock, allowing one less degree of freedom for the model. It can be concluded that the main errors of the final model are related to the amalgamation of the various experiments. This was mostly thought to be related to differences in the k maps, observed when estimating k separately for each flow rate.

This work is of interest to practitioners of reservoir core analysis interested in modeling coreflooding or obtaining detailed permeability maps of the samples. It is also related to a theoretical inverse problem of obtaining k from given saturation and pressure. The latter should be further explored to isolate the source of errors discussed in this work.

Author Contributions: E.A.-D.: Draft preparations, paper figures and diagrams, numerical simulations, manuscript review T.K.: Experimental data acquisition, manuscript review, technical discussions R.P.: Experimental data acquisition, manuscript review, technical discussions A.R.: Draft preparations, manuscript review, technical discussions, supervision. All authors have read and agreed to the published version of the manuscript.

Funding: This work was supported by the Israeli Ministry of Energy.

Informed Consent Statement: All authors have consented for the paper to be published.

Data Availability Statement: The data that support the findings of this study are available from the corresponding author, [AR], upon reasonable request.

Acknowledgments: The authors would like to thank Saurabh Shah for the technical support during the coreflooding experiments.

Conflicts of Interest: The authors declare they have no known financial or personal competing interests that could have appeared to influence the outcome of this research reported in this paper.

References

1. Bickle, M. Geological carbon storage. *Nat. Geosci.* **2009**, *2*, 815. [CrossRef]
2. Cook, P. Clean energy, climate and carbon. *Carbon Manag.* **2012**, *3*, 259–263. [CrossRef]
3. Al-Hashimi, O.; Hashim, K.; Loffill, E.; Marolt Čebašek, T.; Nakouti, I.; Faisal, A.A.; Al-Ansari, N. A comprehensive review for groundwater contamination and remediation: occurrence, migration and adsorption modelling. *Molecules* **2021**, *26*, 5913. [CrossRef] [PubMed]
4. Liu, J.W.; Wei, K.H.; Xu, S.W.; Cui, J.; Ma, J.; Xiao, X.L.; Xi, B.D.; He, X.S. Surfactant-enhanced remediation of oil-contaminated soil and groundwater: A review. *Sci. Total Environ.* **2021**, *756*, 144142. [PubMed]
5. Gautam, P.; Jeong, S.W. Enhanced infiltration of fuel-contaminated hydrophobic unsaturated soil by hydrogen peroxide using surfactant, potassium dihydrogen phosphate, and phytate. *J. Soils Sediments* **2022**, *22*, 1479–1488.
6. Song, B.; Zeng, G.; Gong, J.; Liang, J.; Xu, P.; Liu, Z.; Zhang, Y.; Zhang, C.; Cheng, M.; Liu, Y.; et al. Evaluation methods for assessing effectiveness of in situ remediation of soil and sediment contaminated with organic pollutants and heavy metals. *Environ. Int.* **2017**, *105*, 43–55.
7. Katz, D.; Tek, M. Overview on underground storage of natural gas. *J. Pet. Technol.* **1981**, *33*, 943–951.
8. Kanevskaya, R.; Luré, M.; Maksimov, V.; Filinov, M. Cyclic operation of underground gas store. *J. Eng. Phys.* **1983**, *44*, 452–457. [CrossRef]
9. Oldenburg, C.; Pan, L. Porous media compressed-air energy storage (PM-CAES): Theory and simulation of the coupled wellbore–reservoir system. *Transp. Porous Media* **2013**, *97*, 201–221.
10. Guo, C.; Li, C.; Zhang, K.; Cai, Z.; Ma, T.; Maggi, F.; Gan, Y.; El-Zein, A.; Pan, Z.; Shen, L. The promise and challenges of utility-scale compressed air energy storage in aquifers. *Appl. Energy* **2021**, *286*, 116513.
11. Yortsos, Y.; Chang, J. Capillary effects in steady-state flow in heterogeneous cores. *Transp. Porous Media* **1990**, *5*, 399–420. [CrossRef]
12. Perrin, J.; Benson, S. An experimental study on the influence of sub-core scale heterogeneities on CO_2 distribution in reservoir rocks. *Transp. Porous Media* **2010**, *82*, 93–109. [CrossRef]
13. Krevor, S.; Pini, R.; Li, B.; Benson, S. Capillary heterogeneity trapping of CO_2 in a sandstone rock at reservoir conditions. *Geophys. Res. Lett.* **2011**, *38*. [CrossRef]
14. Ruprecht, C.; Pini, R.; Falta, R.; Benson, S.; Murdoch, L. Hysteretic trapping and relative permeability of CO_2 in sandstone at reservoir conditions. *Int. J. Greenh. Gas Control* **2014**, *27*, 15–27. [CrossRef]
15. Wei, N.; Gill, M.; Crandall, D.; McIntyre, D.; Wang, Y.; Li, K.B.X.; Bromhal, G. CO_2 flooding properties of Liujiagou sandstone: Influence of sub-core scale structure heterogeneity. *Greenh. Gases Sci. Technol.* **2014**, *4*, 400–418.
16. Kuo, C.; Benson, S. Numerical and analytical study of effects of small scale heterogeneity on CO_2/brine multiphase flow system in horizontal corefloods. *Adv. Water Resour.* **2015**, *79*, 1–17.
17. Krevor, S.; Blunt, M.; Benson, S.; Pentland, C.; Reynolds, C.; Al-Menhali, A.; Niu, B. Capillary trapping for geologic carbon dioxide storage–From pore scale physics to field scale implications. *Int. J. Greenh. Gas Control* **2015**, *40*, 221–237.
18. Ni, H.; Boon, M.; Garing, C.; Benson, S.M. Predicting CO_2 residual trapping ability based on experimental petrophysical properties for different sandstone types. *Int. J. Greenh. Gas Control* **2019**, *86*, 158–176.

19. Kong, X.; Delshad, M.; Wheeler, M.F. High Resolution Simulations with a Compositional Parallel Simulator for History Matching Laboratory CO/Brine Coreflood Experiment. In Proceedings of the SPE Reservoir Simulation Symposium, The Woodlands, TX, USA, 18–20 February 2013; Society of Petroleum Engineers: Richardson, TX, USA , 2013.
20. Krause, M.H.; Benson, S.M. Accurate determination of characteristic relative permeability curves. *Adv. Water Resour.* **2015**, *83*, 376–388.
21. Ataie-Ashtiani, B.; Hassanizadeh, A.; Celia, M. Effects of heterogeneities on capillary pressure–saturation–relative permeability relationships. *J. Contam. Hydrol.* **2002**, *56*, 175–192. [CrossRef]
22. Krause, M. Modeling and investigation of the influence of capillary heterogeneity on relative permeability. In Proceedings of the SPE Annual Technical Conference and Exhibition, San Antonio, TX, USA. 8–10 October 2012; Society of Petroleum Engineers: San Antonio, TX, USA, 2012; PE-160909-STU.
23. Rabinovich, A.; Itthisawatpan, K.; Durlofsky, L. Upscaling of CO_2 injection into brine with capillary heterogeneity effects. *J. Pet. Sci. Eng.* **2015**, *134*, 60–75.
24. Rabinovich, A.; Li, B.; Durlofsky, L. Analytical approximations for effective relative permeability in the capillary limit. *Water Resour. Res.* **2016**, *52*, 7645–7667.
25. Jackson, S.J.; Krevor, S. Small-Scale Capillary Heterogeneity Linked to Rapid Plume Migration During CO 2 Storage. *Geophys. Res. Lett.* **2020**, *47*, e2020GL088616.
26. Pentland, C.; El-Maghraby, R.; Iglauer, S.; Blunt, M. Measurements of the capillary trapping of super-critical carbon dioxide in Berea sandstone. *Geophys. Res. Lett.* **2011**, *38* . [CrossRef]
27. Huang, D.D.; Honarpour, M.M. Capillary end effects in coreflood calculations. *J. Pet. Sci. Eng.* **1998**, *19*, 103–117. [CrossRef]
28. Andersen, P.Ø.; Standnes, D.C.; Skjæveland, S.M. Waterflooding oil-saturated core samples-Analytical solutions for steady-state capillary end effects and correction of residual saturation. *J. Pet. Sci. Eng.* **2017**, *157*, 364–379. [CrossRef]
29. Zou, S.; Liu, Y.; Cai, J.; Armstrong, R.T. Influence of capillarity on relative permeability in fractional flows. *Water Resour. Res.* **2020**, *56*, e2020WR027624.
30. Andersen, P.Ø. Analytical modeling and correction of steady state relative permeability experiments with capillary end effects—An improved intercept method, scaling and general capillary numbers. *Oil Gas Sci. Technol.- D'IFP Energies Nouv.* **2021**, *76*, 61.
31. Reynolds, C.; Krevor, S. Characterizing flow behavior for gas injection: Relative permeability of CO2-brine and N2-water in heterogeneous rocks. *Water Resour. Res.* **2015**, *51*, 9464–9489. [CrossRef]
32. Krause, M.; Perrin, J.; Benson, S. Modeling permeability distributions in a sandstone core for history matching coreflood experiments. *SPE J.* **2011**, *16*, 768–777. [CrossRef]
33. Krause, M.; Krevor, S.; Benson, S.M. A procedure for the accurate determination of sub-core scale permeability distributions with error quantification. *Transp. Porous Media* **2013**, *98*, 565–588. [CrossRef]
34. Rabinovich, A.; Anto-Darkwah, E.; Mishra, A. Determining characteristic relative permeability from coreflooding experiments: A simplified model approach. *Water Resour. Res.* **2019**, *55*, 8666–8690. [CrossRef]
35. Leverett, M. Capillary Behavior in Porous Solids. *Trans. AIME* **1941**, *142*, 152–169. [CrossRef]
36. Anto-Darkwah, E.; Rabinovich, A. Modeling imbibition coreflooding in heterogeneous cores with sub-core scale hysteresis. *Adv. Water Resour.* **2022**, *164*, 104214.
37. Jackson, S.J.; Agada, S.; Reynolds, C.A.; Krevor, S. Characterizing drainage multiphase flow in heterogeneous sandstones. *Water Resour. Res.* **2018**, *54*, 3139–3161.
38. Wenck, N.; Jackson, S.J.; Manoorkar, S.; Muggeridge, A.; Krevor, S. Simulating Core Floods in Heterogeneous Sandstone and Carbonate Rocks. *Water Resour. Res.* **2021**, *57*, e2021WR030581. [CrossRef]
39. Kurotori, T.; Pini, R. A general capillary equilibrium model to describe drainage experiments in heterogeneous laboratory rock cores. *Adv. Water Resour.* **2021**, *152*, 103938.
40. Anto-Darkwah, E.; Benson, S.; Rabinovich, A. An improved procedure for sub-core property characterization using data from multiple coreflooding experiments. *Int. J. Greenh. Gas Control* **2021**, *105*, 103226.
41. Dury, O.; Fischer, U.; Schulin, R. A comparison of relative nonwetting-phase permeability models. *Water Resour. Res.* **1999**, *35*, 1481–1493.
42. Richardson, J.; Kerver, J.; Hafford, J.; Osoba, J. Laboratory determination of relative permeability. *J. Pet. Technol.* **1952**, *4*, 187–196.
43. Batycky, J.; McCaffery, F.; Hodgins, P.; Fisher, D. Interpreting relative permeability and wettability from unsteady-state displacement measurements. *Soc. Pet. Eng. J.* **1981**, *21*, 296–308.
44. Berg, S.; Oedai, S.; Ott, H. Displacement and mass transfer between saturated and unsaturated CO_2–brine systems in sandstone. *Int. J. Greenh. Gas Control* **2013**, *12*, 478–492. [CrossRef]
45. Moreno, Z.; Rabinovich, A. Impact of Sub-core-scale Heterogeneity on Meter-Scale Flow and Brine Displacement in Drainage by CO_2. *Water Resour. Res.* **2021**, *57*, e2020WR028332. [CrossRef]
46. Hejazi, S.A.H.; Shah, S.; Pini, R. Dynamic measurements of drainage capillary pressure curves in carbonate rocks. *Chem. Eng. Sci.* **2019**, *200*, 268–284.
47. Pini, R.; Benson, S.M. Simultaneous determination of capillary pressure and relative permeability curves from core-flooding experiments with various fluid pairs. *Water Resour. Res.* **2013**, *49*, 3516–3530.
48. Akin, S.; Kovscek, A. Computed tomography in petroleum engineering research. *Geol. Soc. London Spec. Publ.* **2003**, *215*, 23–38.

49. Van Genuchten, M.T. A closed-form equation for predicting the hydraulic conductivity of unsaturated soils. *Soil Sci. Soc. Am. J.* **1980**, *44*, 892–898. [CrossRef]
50. Brooks, R.; Corey, A. Properties of porous media affecting fluid flow. *J. Irrig. Drain. Div.* **1966**, *92*, 61–90. [CrossRef]
51. Cao, H. Development of Techniques for General Purpose Simulators. Ph.D. Thesis, Stanford University Stanford, Stanford, CA, USA, 2002.
52. Virnovsky, G.; Friis, H.; Lohne, A. A steady-state upscaling approach for immiscible two-phase flow. *Transp. Porous Media* **2004**, *54*, 167–192. [CrossRef]
53. Moreno, Z.; Anto-Darkwah, E.; Rabinovich, A. Semi-Analytical Modeling of Rate-Dependent Relative Permeability in Heterogeneous Formations. *Water Resour. Res.* **2021**, *57*, e2021WR029710.
54. Moreno, Z.; Rabinovich, A. Evaluating numerical simulation errors of CO_2-brine flow with capillary heterogeneity using a 1D semi-analytical solution. *Int. J. Greenh. Gas Control* **2021**, *110*, 103416. [CrossRef]